Click Here for Full Article

Seismic evidence for large-scale compositional heterogeneity of oceanic core complexes

J. Pablo Canales and Brian E. Tucholke
Department of Geology and Geophysics, Woods Hole Oceanographic Institution, MS 24, 360 Woods Hole Road, Woods Hole, Massachusetts 02543, USA (jpcanales@whoi.edu)

Min Xu
Massachusetts Institute of Technology–Woods Hole Oceanographic Institution Joint Program, Woods Hole, Massachusetts 02543, USA

John A. Collins and David L. DuBois
Department of Geology and Geophysics, Woods Hole Oceanographic Institution, MS 24, 360 Woods Hole Road, Woods Hole, Massachusetts 02543, USA

[1] Long-lived detachment faults at mid-ocean ridges exhume deep-seated rocks to form oceanic core complexes (OCCs). Using large-offset (6 km) multichannel seismic data, we have derived two-dimensional seismic tomography models for three of the best developed OCCs on the Mid-Atlantic Ridge. Our results show that large lateral variations in P wave velocity occur within the upper $\sim 0.5-1.7$ km of the lithosphere. We observe good correlations between velocity structure and lithology as documented by in situ geological samples and seafloor morphology, and we use these correlations to show that gabbros are heterogeneously distributed as large (tens to >100 km^2) bodies within serpentinized peridotites. Neither the gabbros nor the serpentinites show any systematic distribution with respect to along-isochron position within the enclosing spreading segment, indicating that melt extraction from the mantle is not necessarily focused at segment centers, as has been commonly inferred. In the spreading direction, gabbros are consistently present toward the terminations of the detachment faults. This suggests enhanced magmatism during the late stage of OCC formation due either to natural variability in the magmatic cycle or to decompression melting during footwall exhumation. Heat introduced into the rift valley by flow and crystallization of this melt could weaken the axial lithosphere and result in formation of new faults, and it therefore may explain eventual abandonment of detachments that form OCCs. Detailed seismic studies of the kind described here, when constrained by seafloor morphology and geological samples, can distinguish between major lithological units such as volcanics, gabbros, and serpentinized peridotites at lateral scales of a few kilometers. Thus such studies have tremendous potential to elucidate the internal structure of the shallow lithosphere and to help us understand the tectonic and magmatic processes by which they were emplaced.

1. Introduction

[2] Oceanic core complexes (OCCs) are deep sections of the oceanic lithosphere exhumed to the seafloor by long-lived detachment faults [*Cann et al.*, 1997; *MacLeod et al.*, 2002; *Tucholke et al.*, 1998]. When active, these faults constitute the sole extensional boundary between separating tectonic plates [*deMartin et al.*, 2007; *Smith et al.*, 2006; *Tucholke et al.*, 1998], and in some instances they can accommodate extension for 1–2 Ma forming relatively smooth-surfaced, dome-shaped megamullions due to footwall rollover [*Tucholke et al.*, 1996, 1998]. These features commonly exhibit spreading-parallel corrugations or "mullions" that can have amplitudes up to several hundred meters, and they have been identified at a wide variety of spreading centers [*Cannat et al.*, 2006; *Ohara et al.*, 2001; *Okino et al.*, 2004; *Searle et al.*, 2003; *Tucholke et al.*, 1998, 2008].

[3] The abundance of gabbros and peridotites recovered in most OCCs [*Blackman et al.*, 2002, 2006; *Cann et al.*, 1997; *Dick et al.*, 2000, 2008; *Escartín et al.*, 2003; *MacLeod et al.*, 2002; *Reston et al.*, 2002; *Tucholke and Lin*, 1994], together with gravity modeling that suggests the presence of mantle-like densities near the seafloor [e.g., *Nooner et al.*, 2003], indicates that OCCs may be ideal tectonic windows where the geological record of mantle flow and melt generation and migration can be studied [*Tucholke et al.*, 1998]. They also have the potential for hosting serpentinite-based hydrothermal systems [*Früh-Green et al.*, 2003; *Kelley et al.*, 2001]. However, the relative abundances and distribution of these lithologies are not well constrained. Drilling at OCCs to date has recovered dominantly gabbroic rocks [*Blackman et al.*, 2006; *Dick et al.*, 2000; *Kelemen et al.*, 2004], raising a question of the extent to which OCCs actually provide access to the oceanic mantle. Thus the origin and evolution of OCCs, their significance as tectonic windows into the oceanic lithosphere, and their potential as widespread hosts of serpentinite-based hydrothermal ecosystems remain uncertain.

[4] In this paper we present seismic tomography images obtained across three of the best developed and best studied OCCs on the Mid-Atlantic Ridge

(MAR): Kane [*Dick et al.*, 2008; *Tucholke et al.*, 1998], Dante's Domes [*Tucholke et al.*, 2001], and Atlantis [*Cann et al.*, 1997] (Figure 1). The tomography models reveal large lateral variations in *P* wave velocity within the shallow lithosphere beneath all three OCCs, as well as distinctly different velocity structure in the associated volcanic hanging walls. A strong correlation between the modeled velocity variations and lithology of in situ geological samples allows us to constrain the large-scale spatial distribution of gabbroic intrusions and serpentinized peridotites within the OCCs, thus providing valuable new insights into the formation and evolution of these features.

2. Geological Settings

[5] The three OCCs studied show characteristic smooth surfaces and spreading-parallel corrugations typical of megamullions formed by major oceanic detachment faults [*Tucholke et al.*, 1998]. Hereinafter we use *Tucholke et al.*'s [1998] definitions of breakaway zone (where the faults initially nucleated) and termination of the faults. Breakaway zones are generally defined by isochron-parallel ridges that mark the older limit of fault corrugations; however, early corrugations often are not well developed and this limit can be difficult to determine. Terminations are more easily identified because they mark the young limit of a smooth, corrugated fault surface against rougher adjacent terrain of the hanging wall.

2.1. Kane Oceanic Core Complex

[6] Kane OCC is located between ∼30 and 55 km off-axis on the North American plate immediately south of the Kane Transform Fault (TF), between ∼23°20′N and ∼23°40′N (Figure 1). It formed between 3.3 Ma and 2.1 Ma under conditions of strongly asymmetrical spreading (17.9 mm a^{-1} on the OCC side to the west, and 7.9 mm a^{-1} on the conjugate between Chrons 2 and 2A [*Williams et al.*, 2006]). The breakaway for this OCC is marked by a linear ridge that is continuous for more than 35 km along isochron (with the possible exception of a small offset near latitude 23°30′N, Figure 1). The detachment fault constituting the surface of the OCC exhibits several domes (Babel, Abel, Cain,
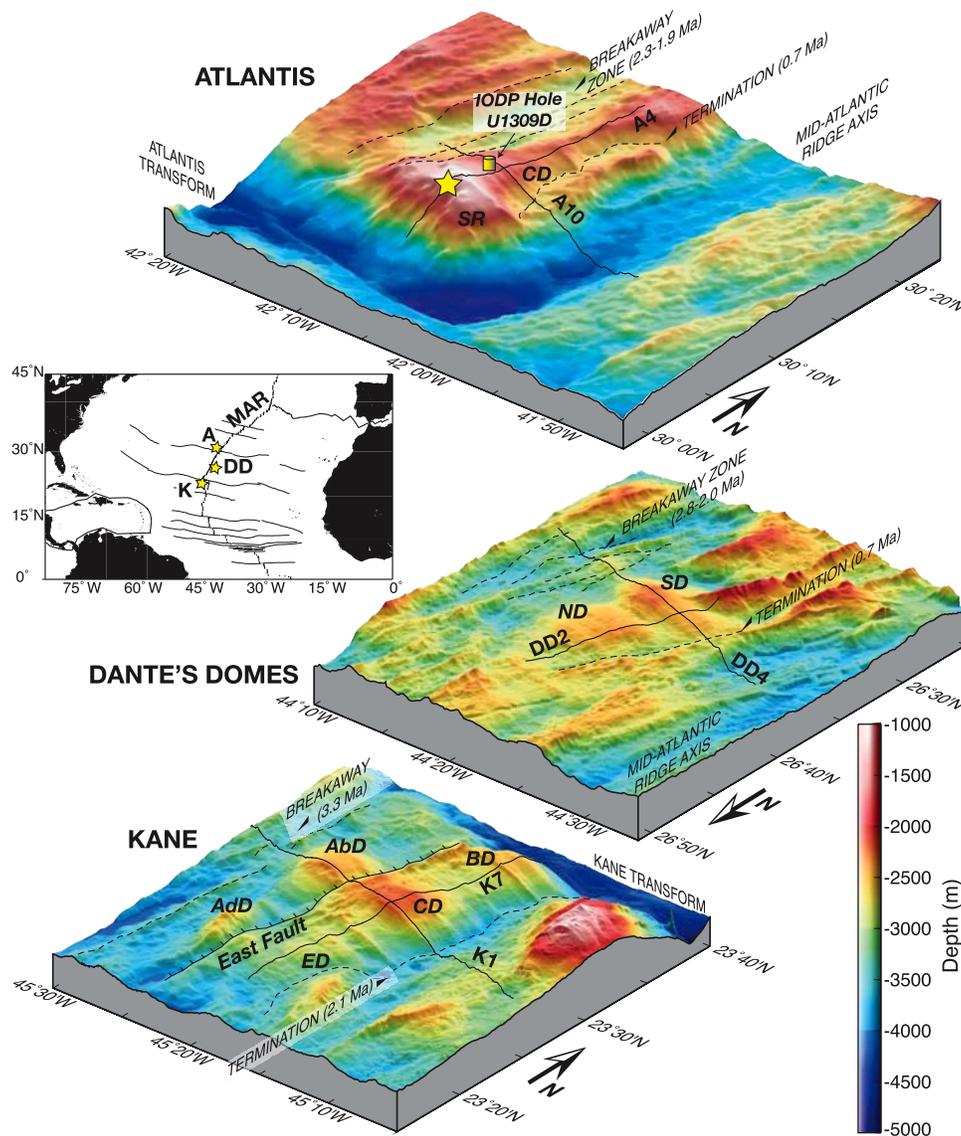
Figure 1. Shaded-relief, three-dimensional perspectives of multibeam bathymetry over Atlantis, Kane, and Dante's Domes OCCs. (Note the different view angle of the Dante's Dome image). Solid lines locate seismic profiles (numbered with A, DD, and K). Dashed lines show locations of breakaways and terminations of detachment faults. SR and CD are the Southern Ridge and Central Dome, respectively, of Atlantis OCC; ND and SD are the northern and southern domes, respectively, of Dante's Domes OCC; and AD, BD, CD, and ED are the Abel, Babel, Cain, and Eve domes, respectively, of Kane OCC. Yellow star on Atlantis OCC locates the Lost City hydrothermal field. The inset at left shows the location of the three OCCs on the flanks of the MAR in the northern central Atlantic.

Adam, and Eve, following the nomenclature of *Dick et al.* [2008]) and is cut by a large-offset, high-angle, west-facing normal fault (East Fault, labeled in Figure 1). Extensive geological sampling indicates that the central and western parts of the Kane OCC are predominantly ultramafic [*Dick et al.*, 2008]. Both peridotites and gabbros are exposed along the northern edge of the OCC (south wall of the Kane TF) [*Auzende et al.*, 1994]. Slide scars along East Fault expose massive outcrops of

serpentinized peridotite at the center of the OCC, providing direct evidence of the footwall composition there [*Dick et al.*, 2008].

2.2. Dante's Domes Oceanic Core Complex

[7] Dante's Domes OCC lies just east of the MAR rift valley on the African plate, between ~26°32′N and ~26°40′N, away from any major segment discontinuity [*Tucholke et al.*, 2001] (Figure 1). Total spreading rate in the area during formation of

the OCC was ~22 mm a^{-1} [*DeMets et al.*, 1990]. A set of ridges near the eastern limit of the OCC defines a broad breakaway zone, located in 2.0–2.8 Ma lithosphere. To the west, the detachment surface is terminated by an oblique set of valleys and ridges created by a rift that propagated southward between ~1.3 and 0.7 Ma. The OCC exhibits two domes that are adjacent along strike. Submersible dives show that dominantly allochthonous basalt debris and minor serpentinite is scattered across the corrugated detachment surface. There are no direct constraints on composition of the footwall, but gravity modeling indicates densities consistent with gabbros and/or partially serpentinized peridotites [*Tucholke et al.*, 2001].

2.3. Atlantis Oceanic Core Complex

[8] Atlantis OCC lies just west of the MAR rift valley immediately north of Atlantis TF, between ~30°05′N and ~30°17′N (Figure 1), where the full spreading rate is ~24 mm a^{-1} [*Sempéré et al.*, 1995]. The location of the breakaway is ambiguous, but it is most likely located within a zone limited by two north-south trending ridges (Figure 1) in 2.3–1.9 Ma lithosphere. The termination is marked by a contact between the smooth corrugated detachment surface and a basaltic hanging wall block in ~0.7 Ma lithosphere that forms the western shoulder of the rift valley [*Blackman et al.*, 2002; *Tucholke et al.*, 1998]. Atlantis OCC has two main morphological units [*Blackman et al.*, 2002]: the Central Dome and the elevated Southern Ridge along the top of the northern wall of Atlantis TF (Figure 1). Spreading-parallel corrugations are best developed on the Central Dome. The southern part of the Central Dome was drilled at Hole U1309D during IODP Expeditions 304 and 305 (Figure 1) and ~1415 m of predominantly gabbroic rocks were recovered [*Blackman et al.*, 2006; *Ildefonse et al.*, 2007]. In contrast, large slide scars along the southern flank of the Southern Ridge, where the Lost City serpentinite-hosted hydrothermal system is located [*Kelley et al.*, 2001], expose massive outcrops of serpentinized peridotite with lesser gabbro [*Karson et al.*, 2006].

3. Data and Methods

3.1. Data Acquisition and Processing

[9] The multichannel seismic data used in this study were acquired in 2001 aboard R/V *Maurice Ewing* (cruise EW0102) using a 6-km-long, 480-channel Syntron digital hydrophone streamer towed at a nominal depth of 10 m. Hydrophone group (i.e., receiver) spacing was 12.5 m. The sound source was a tuned, 10-element air gun array with a total capacity of 51 L (3100 in^3) triggered by distance every 37.5 m and towed at a nominal depth of 8 m. Data were recorded in 10-s long records sampled every 4 ms. Positions of sources and receivers were derived from shipboard and tail-buoy GPS receivers and compass-enhanced DigiCourse birds placed along the streamer. The long-offset hydrophone streamer and the shallow depths of the OCCs allowed recording of subseafloor refractions that we use to derive the two-dimensional seismic velocity structure beneath the exposed detachment-faults surfaces using traveltime tomography methods.

[10] Six profiles were acquired at the Kane OCC, three profiles at Dante's Domes OCC, and five profiles across Atlantis OCC. In this paper we present results from profiles that best sample the main morphological features of the OCCs, i.e., two profiles that cross each of the corrugated surfaces along dip and strike directions (Figure 1). Results from the complete set of the Kane profiles support the results presented here and provide a more detailed view of the Kane OCC [*Xu et al.*, 2007]; those results will be published elsewhere. The remaining profiles of the Atlantis OCC have yet to be modeled and will be published elsewhere.

[11] Shot gathers exhibit clear subseafloor refractions (Figure 2) and only minimum processing was required for this study. Bad traces were edited, and every five consecutive shots were gathered and the common-offset traces were stacked and averaged to form 480-fold "super shot gathers" in order to improve the signal-to-noise ratio (SNR). The super shot gathers were filtered in the frequency-wave number domain to remove low-frequency cable noise. Traveltime picks were done in band-pass filtered super shot gathers with frequency bands of 3-5-15-30 Hz or 3-5-30-50 Hz, depending on the data quality. Traveltime uncertainty was assigned on the basis of the SNR in a 100-ms window before and after the pick [*Zelt and Forsyth*, 1994]. Although traveltimes were picked in all of the super shot gathers where subseafloor refractions were observed, traveltime picks were decimated in the shot and receiver domains before the inversion. Decimation of the traveltimes was done primarily because the complete data set has a higher lateral sampling than can be resolved by traveltime tomography. Ray theory limits the lateral resolution to the first Fresnel zone [e.g., *Yilmaz*, 1987]. In our
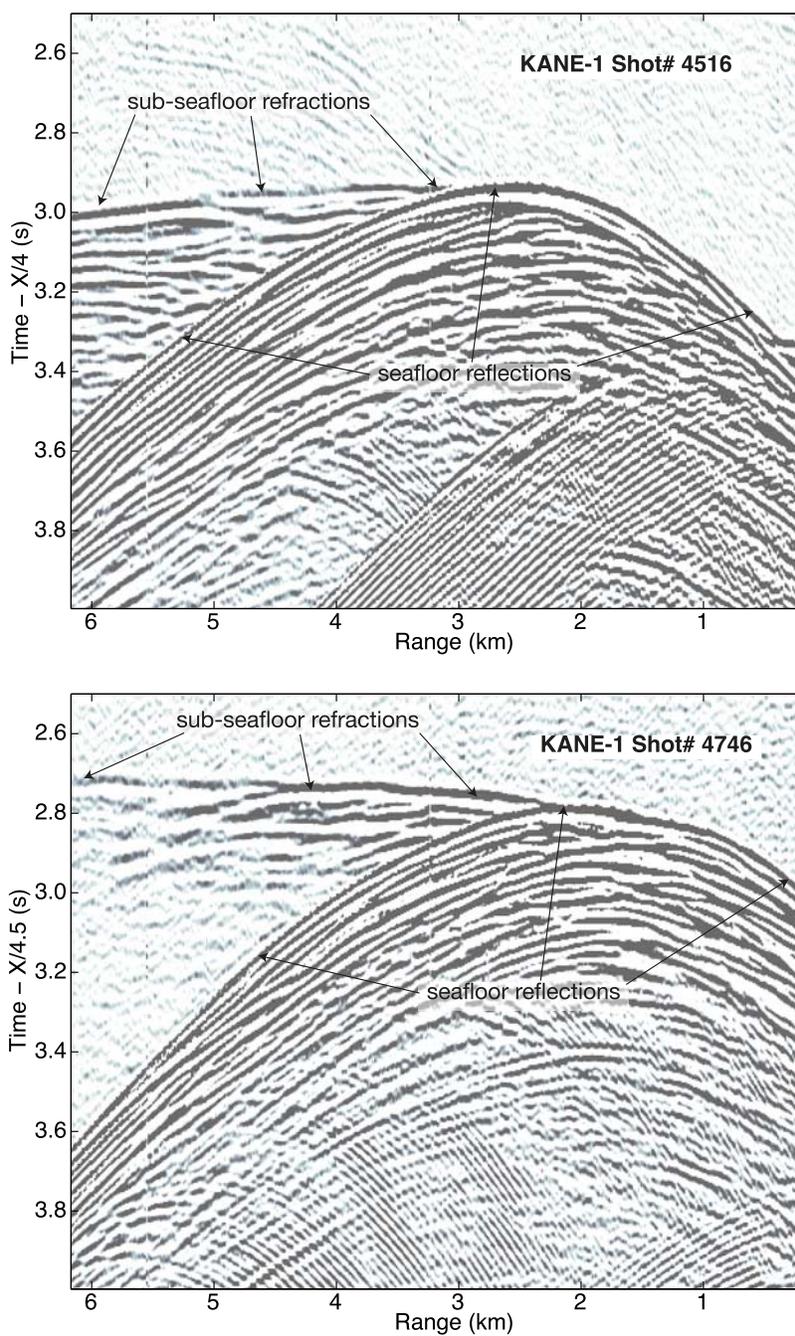
Figure 2. Representative shot gathers from profile K1 over the Kane OCC. Horizontal axes are distances from source to receivers along the streamer, and vertical axes are reduced two-way traveltime (reduction velocities of 4 km s^{-1} and 4.5 km s^{-1}, top and bottom, respectively).

case, the first Fresnel zone at an average seafloor depth of 2.5 km is 250 m for a dominant frequency of 30 Hz (deeper below the seafloor the Fresnel zone increases as the dominant frequency in the data decreases and the propagation length increases). Therefore we used traveltime picks from one out of every 5 shot gathers (i.e., effective source spacing of 187.5 m), and from one out of every 10 receivers

within each shot gather (i.e., effective receiver spacing of 125 m). The decimated set of tra veltime picks is shown in Figure 3 as color maps of traveltime versus shot number and source-receiver offset.

[12] Feathering of the streamer was minimal and ranged between ~6° (profile K7) and ~3° (profiles
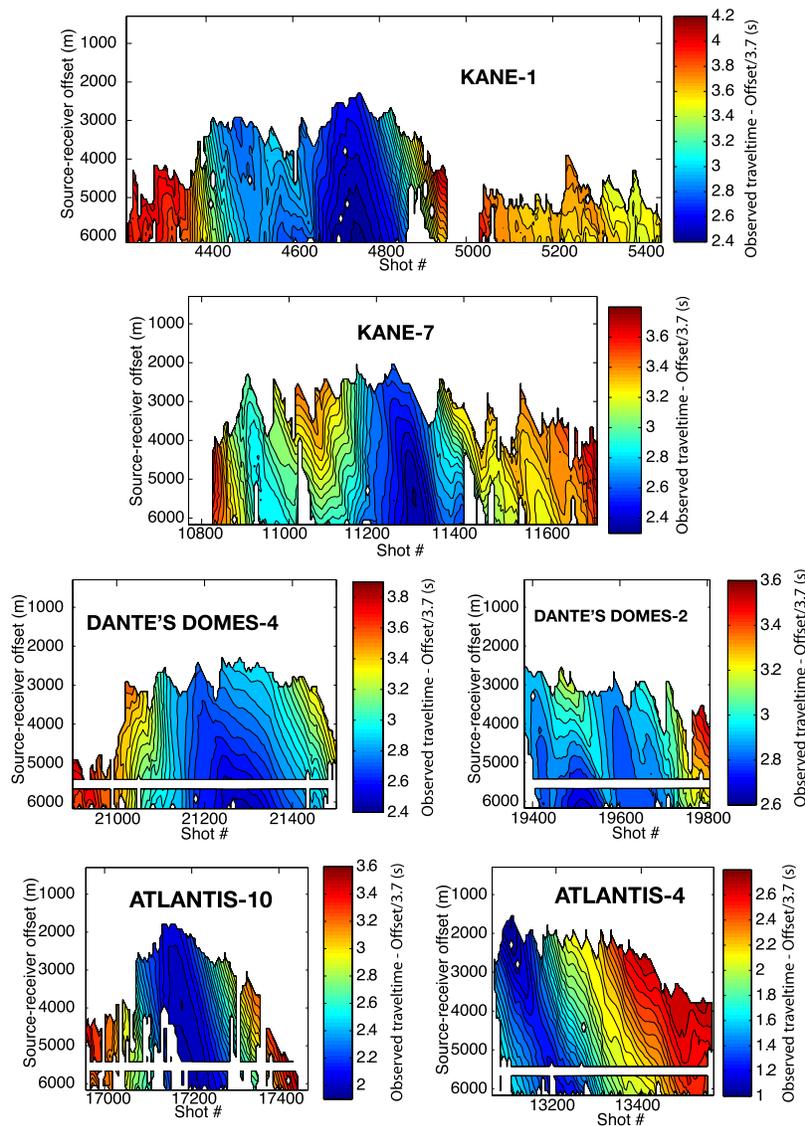
Figure 3. Color plots showing observed traveltime picks (two-way traveltime reduced at 3.7 km s^{-1}) displayed as a function of shot number and source-receiver offset for each of the seismic profiles. White areas indicate that no traveltimes were picked for a particular shot-receiver pair because of noisy data or because subseafloor refractions arrive later than the seafloor reflection at short offsets.

K1 and A4), resulting in receivers being off the ideal two-dimensional profile by a maximum of ~650 m at the largest offsets. (Feathering was not possible to calculate for profile A10 owing to corrupted readings by the streamer tail buoy GPS; for this profile we assumed that all of the sources and receivers were perfectly aligned along the profile.) Projection of these out-of-plane receiver locations into a 2-D profile does not introduce significant uncertainty in the observed traveltimes because the differences between the true and projected source-receiver offsets are less than ~35 m, on the same order as the grid spacing

used for raypath and traveltime calculations (see next section). Perhaps the most important influence of streamer feathering in our results is the three-dimensional structure in the vicinity of the profiles that cannot be modeled with our approach. For example, the deepest parts of the tomography models are most sensitive to feathering because they are constrained by the largest offsets; therefore they probably represent an average structure within a few hundred meters of the profile in the cross-line direction.
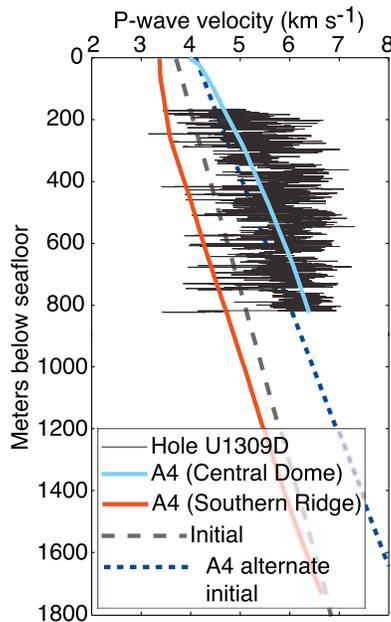
Figure 4. One-dimensional velocity structures at Atlantis OCC extracted from profile A4 beneath the Central Dome at the location closest to Hole U1309 (blue) and beneath the Southern Ridge at −9.5 km model distance (red). Solid black line shows sonic-log velocities measured in situ within the upper ∼200–800 m of IODP Hole U1309D [*Blackman et al.*, 2006]. Long-dash gray line shows the initial velocity model used in our tomography inversions. Short-dash blue line shows an alternate initial velocity model for profile A4 that was used to obtain the results shown in Figure 11.

3.2. Streamer Traveltime Tomography

[13] Traveltime tomography models were obtained using the software FAST [*Zelt and Barton*, 1998]. The forward problem (ray tracing and traveltime calculation) was solved in a regular grid with 25 m node spacing both vertically and horizontally. Because most of the subcrustal refractions observed in our data are not true first arrivals (a common requirement in most traveltime tomography methods) owing to the deep-water environment (first arrivals in our data correspond to the direct wave propagating horizontally from sources to receivers through the water), the ray tracing algorithm was modified in order to calculate raypaths and traveltimes from subseafloor arrivals.

[14] The nonlinear inverse problem was solved using a regularized, damped least squares solution. The inverse model was parameterized as a regular grid with 200 m node spacing both vertically and horizontally. This grid spacing was chosen to be of

the same order as the first Fresnel zone at the seafloor (see previous sections) to avoid over-parameterizing the inverse problem. As a starting velocity model we used a laterally invariant model with constant vertical velocity gradient that best represents the one-dimensional structure of the Kane OCC [*Xu et al.*, 2007] (3.7 km s^{-1} at the seafloor and vertical gradient of 1.75 s^{-1} below the seafloor, Figure 4). Regularization was achieved by minimizing an objective function dependent on the traveltime residuals (weighted by their uncertainty) and the second spatial partial derivatives of the model parameters [*Zelt and Barton*, 1998]. Readers should note that minimizing the second spatial derivatives of the model parameters results in models that have minimum roughness and therefore deviate as little as possible from the linear velocity gradient of the starting model.

[15] The trade-off between minimizing data residuals or obtaining a smooth solution is controlled by the damping parameter λ [*Zelt and Barton*, 1998]. We ran inversions with different values of λ, and at each of the three study areas we selected the results that provided a weighted traveltime misfit function $\chi^2 \leq 1.1$ in the minimum number of iterations (Figure 5). Our preferred solutions are shown in Figure 6, and they correspond to the second iteration with $\lambda = 20$ at the Atlantis and Dante's Domes sites, and $\lambda = 10$ at the Kane site (5 iterations were run in all cases). The importance of horizontal versus vertical smoothing constraints is controlled by the parameter s_z [*Zelt and Barton*, 1998], with $s_z = 0$ indicating no smoothing is imposed in the vertical direction, $s_z = 1$ meaning roughness of model is equal both along vertical and horizontal directions, and $s_z > 1$ resulting in models with stronger smoothing constraints in the vertical direction. We found that our results were not significantly sensitive to values of $s_z < 0.075$, while larger values resulted in large χ^2 misfits, so we used $s_z = 0.075$ in all of the inversions.

[16] The strong lateral variations in velocity along the profiles (Figure 6) are required by, and not simply consistent with, the observed data. For example, Figure 7 shows results for profile K1 that include observed seismograms, traveltime picks, raypaths, and predicted traveltime curves for two representative shot gathers that sample very different velocity structures. The initial velocity model accurately predicts the observed traveltimes for shot# 4516, but predicts traveltimes that are too large for shot# 4746, demonstrating the presence of large lateral velocity variations. Figure 7 also
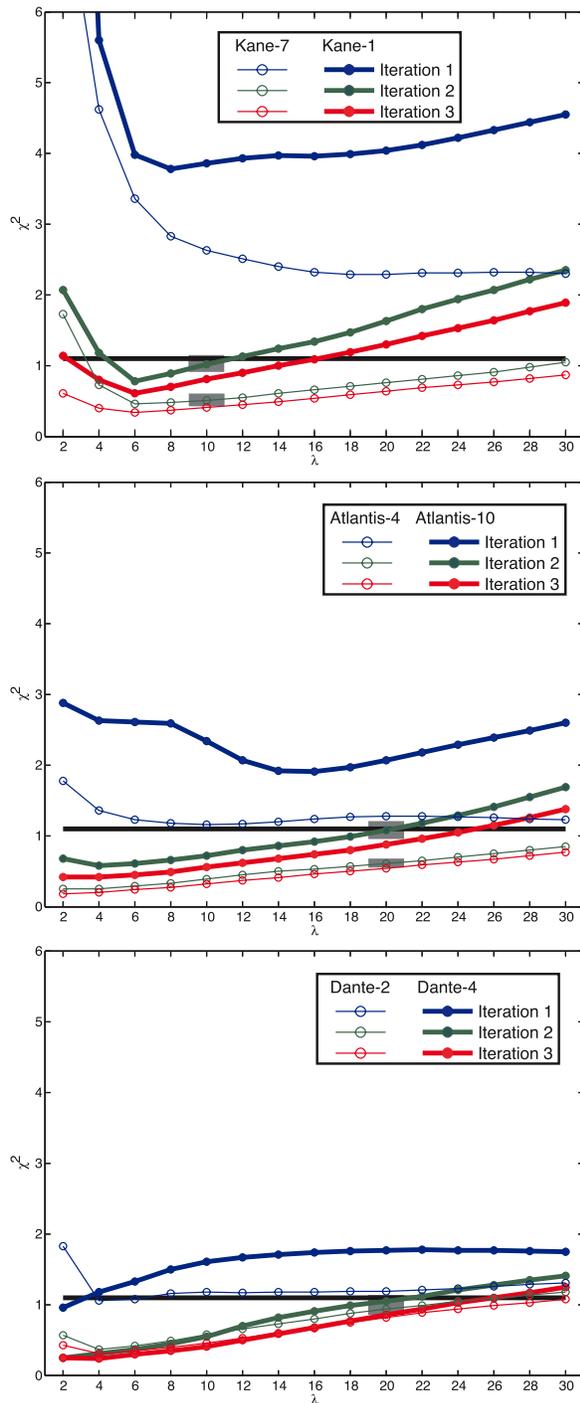
Figure 5. Variation in misfit function between observed and predicted traveltimes as a function of damping parameter λ, for several inversion iterations. Gray squares indicate the preferred solutions shown in Figure 6. Black line corresponds to $\chi^2 = 1.1$, the adopted threshold value for the misfit function.

shows the complete ray coverage for profile K1. This example shows that ray coverage is dense and relatively homogeneous along the profiles.

[17] The large negative and positive traveltime residuals predicted by the initial velocity model are reduced to significantly lower residuals by the final models (Figure 8). Data are generally equally well fitted across all source-receiver offsets and shots, particularly for profiles K1, K7, and A10 (Figure 9), except at some locations where topography is rougher and/or seafloor deeper (e.g., near shot 5200 in profile K1, Figure 9). However, profiles A4, DD2, and DD4 show some dependence of traveltime residuals on source-receiver offset, with positive residuals appearing at near offsets and negative residuals at large offsets (Figure 9). This indicates that although the preferred models provide a satisfactory statistical fit to the observations and their uncertainties, the models do not fully capture the complexity and small-scale subseafloor heterogeneities that are likely to be present beneath the OCCs. Thus, our results should be seen as one possible solution to the non-unique inverse problem, representing the minimum large-scale structure that is needed to fit the data within the imposed smoothing constraints. Other approaches such as those of *Harding et al.* [2007] that incorporate into the inversion the traveltimes from the nearest offsets (not used in this study; see Figure 3), or high-resolution waveform tomography of streamer data [e.g., *Shipp and Singh*, 2002], will be needed to improve vertical resolution and better characterize the structure of OCCs, particularly within their shallow most (<200 m) parts.

3.3. Resolution Tests

[18] We conducted several tests to assess the lateral resolution of the final velocity models. We created synthetic velocity models by adding alternating positive and negative vertical anomalies to the initial model shown in Figure 4. The amplitudes of the anomalies varied laterally between ±0.5 km s^{-1} following a sinusoidal function. Tests were done for anomalies with different widths (i.e., half wavelength of the sinusoidal perturbation) ranging from 1.5 km to 5.0 km. Synthetic traveltimes were calculated for each of the synthetic models using the same experimental geometry as in our seismic profiles. We then inverted the calculated traveltimes using the same parameters as in our tomography inversion. Only one iteration was required to achieve the desired misfit of $\chi^2 \leq 1.1$. Results from profiles K1 and K7, which are representative
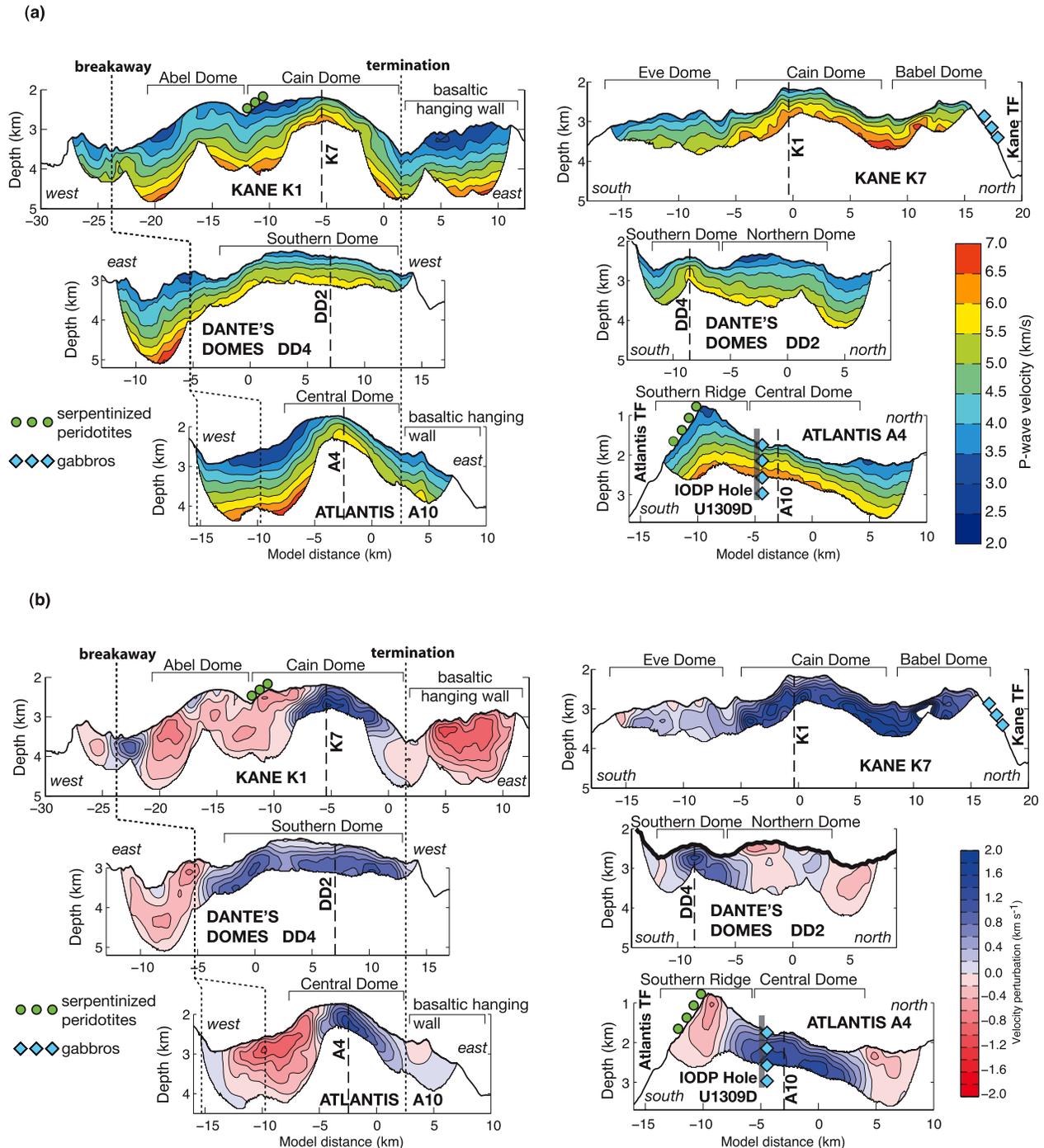
Figure 6. (a) Two-dimensional tomography models of *P* wave velocity beneath Kane, Dante's Domes, and Atlantis OCCs (profile locations in Figure 1). Contours are every 0.5 km s^{-1}. Left panels are dip profiles, and right panels are strike profiles. Short-dashed lines on dip profiles indicate locations of breakaways and terminations. Long-dashed lines show crossings between dip and strike profiles. Green dots and blue diamonds (serpentinite and gabbro, respectively) show dominant in situ lithologies sampled by submersible or remotely operated vehicle [*Auzende et al.*, 1994; *Dick et al.*, 2008; *Karson et al.*, 2006] or drilled [*Blackman et al.*, 2006] (IODP Hole U1309D, vertical gray line projected onto profile A4). (b) Same as Figure 6a with models shown as perturbations with respect to the initial one-dimensional velocity model (Figure 4), with contours every 0.2 km s^{-1}.
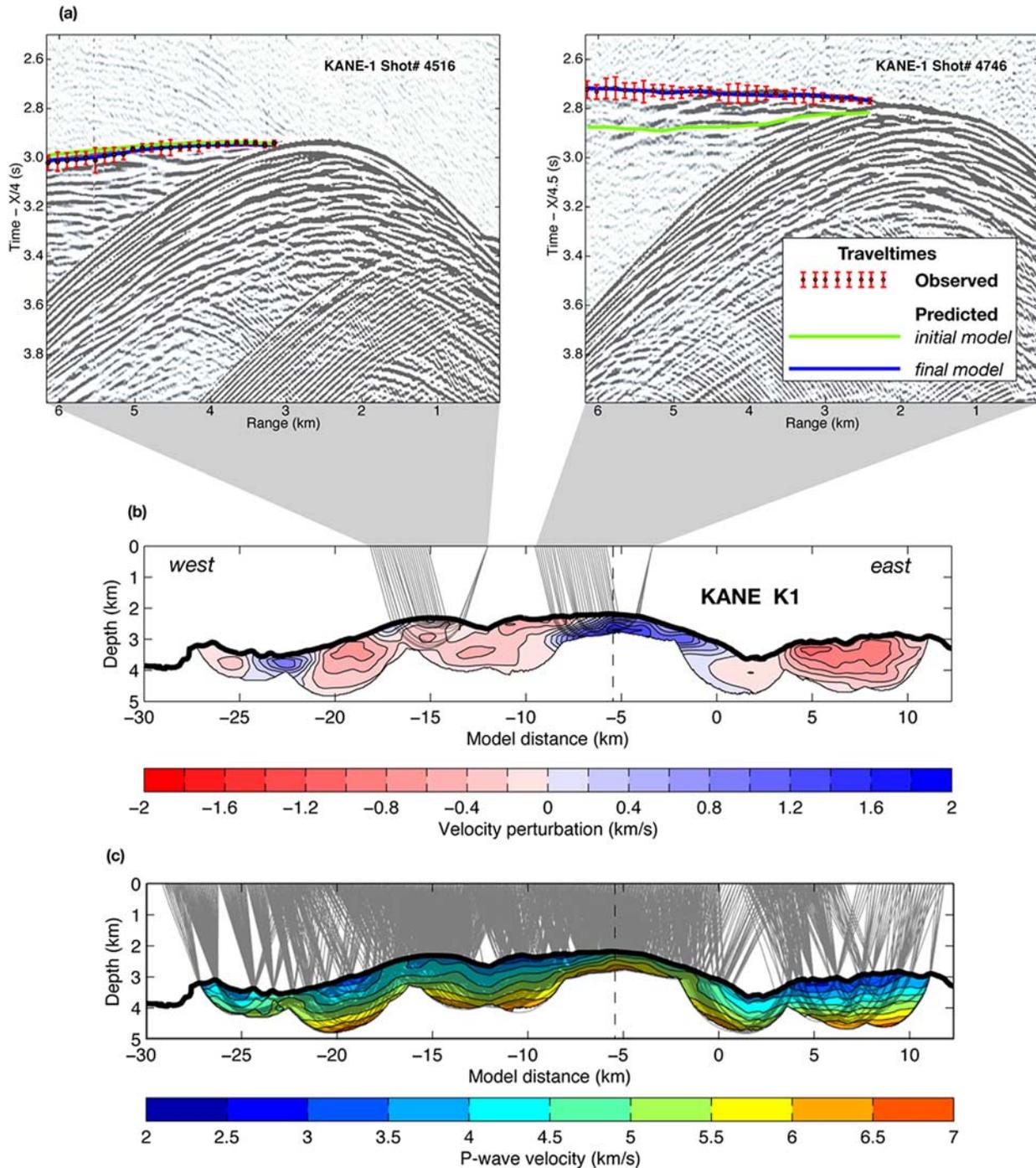
Figure 7. (a) Shot gathers from Figure 2 with observed traveltimes and their assigned uncertainty (circles with red error bars). Traveltime curves are shown as predicted by the initial model (green, from Figure 4) and the final model in Figure 6 (blue). (b) Final velocity model for profile K1, shown as perturbations with respect to the initial model, and contoured every 0.2 km s^{-1}. Raypaths (gray lines) for the two source-receiver pairs in Figure 7a, above, are shown. (c) Final velocity model for profile K1 with complete ray coverage and contours every 0.5 km s^{-1}.
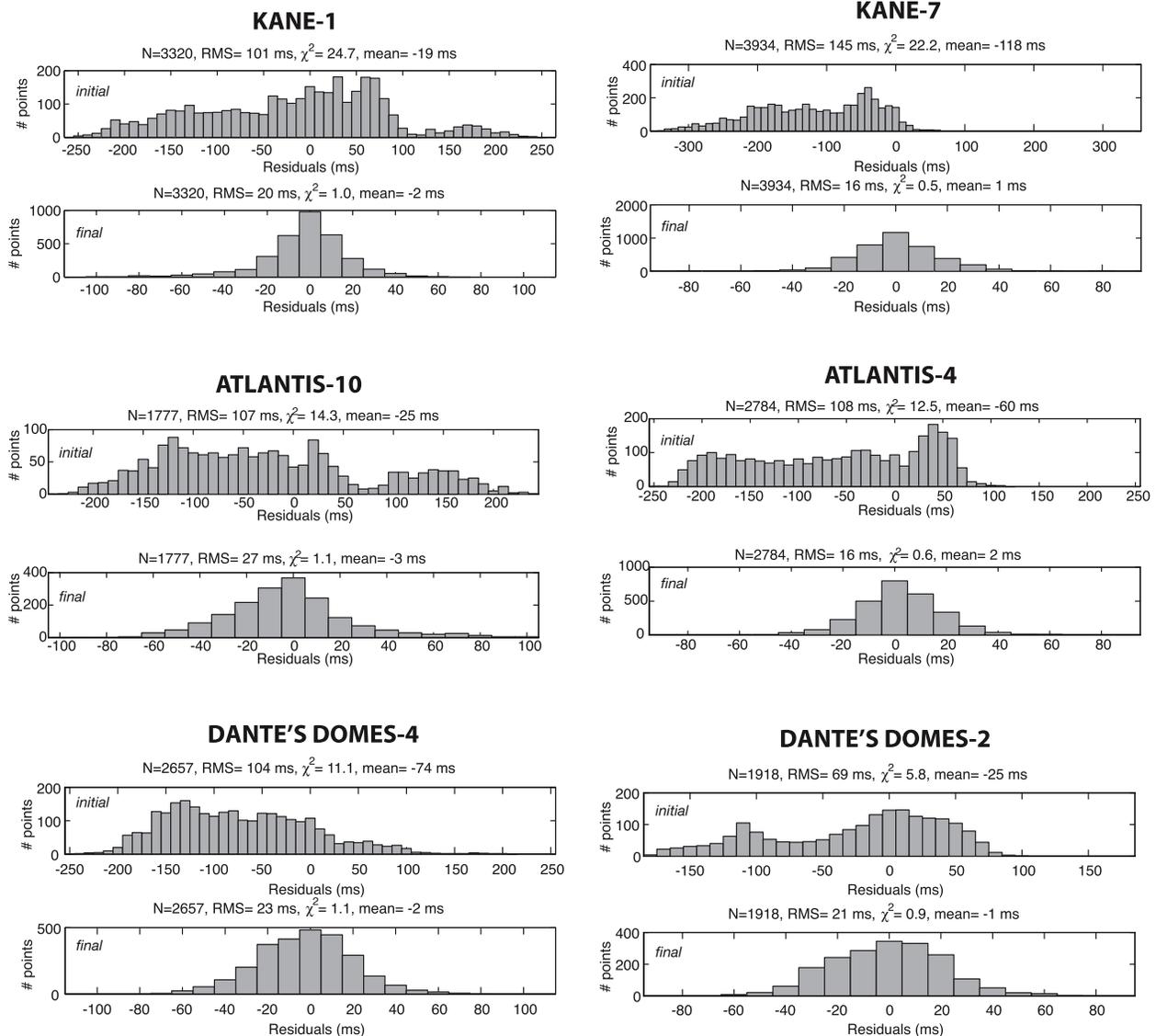
Figure 8. Traveltime residual histograms. Results of both initial and final models are shown for each seismic profile. N indicates number of observations, RMS is root-mean squared, χ^2 is weighted misfit function, and mean is the mean of the distributions.

for all the other profiles, are shown in Figure 10. The tests indicate that along sections of profile K1 where seafloor is shallowest, features as small as 1.5 km wide in the final velocity model (Figure 6) are meaningful and well resolved at subseafloor depths less than ~0.5 km (Figure 10a). Along other parts of the profile where seafloor is deeper, only anomalies that are larger than 2.0–2.5 km wide above ~0.5 km subseafloor depth should be trusted and interpreted. At subseafloor depths greater than 0.5 km, only features at scales of 5 km or larger along profile K1 are meaningful. Similar results were found for profile K7 (Figure 10b), although in

this case the tests indicated that anomalies smaller than 2.5 km were not resolved in the final model.

4. Results

4.1. Seismic Structure

[19] Our tomography models reveal strong lateral gradients in P wave velocity at scales of 1 km or less within the upper ~0.5–1.7 km of the lithosphere across the three OCCs (Figure 6). Velocities are everywhere greater than 3 km s^{-1} but rarely exceed 6 km s^{-1}. We group velocity structures into three classes that commonly are separated by the
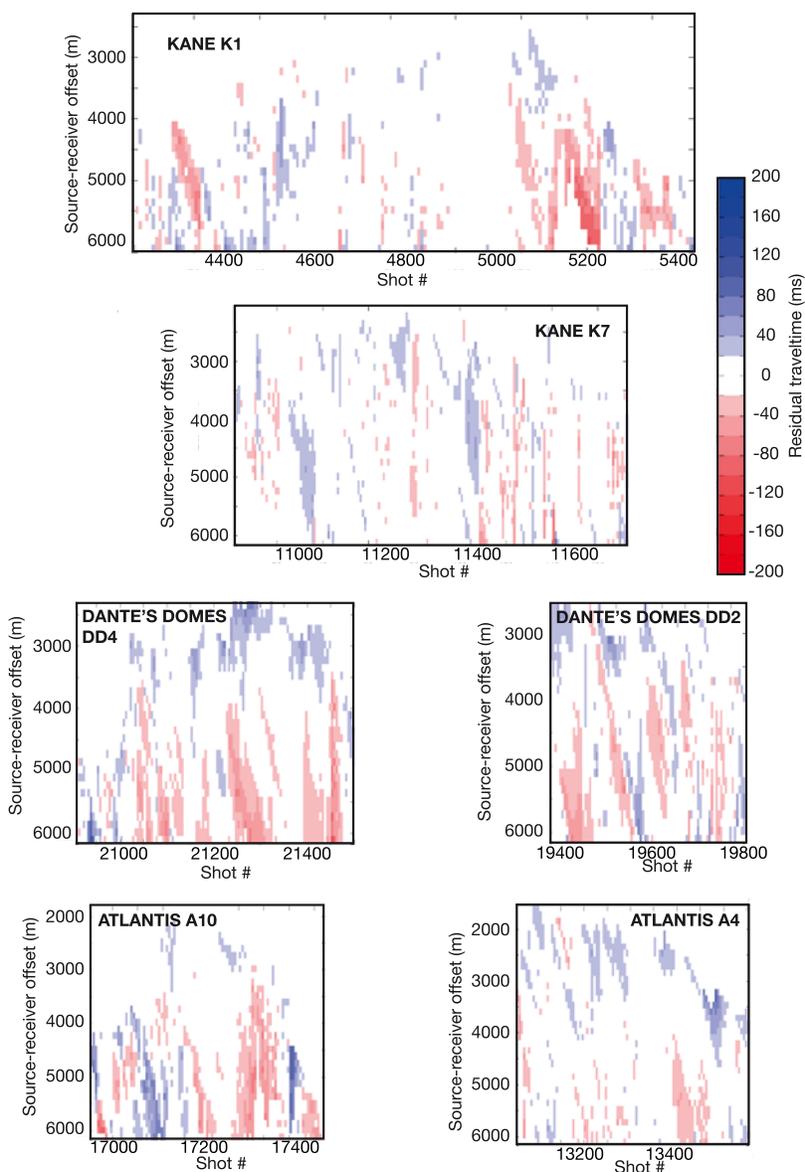
Figure 9. Color plots showing residual traveltimes predicted by the final models displayed as a function of shot number and source-receiver offset for each of the seismic profiles.

transitions noted above. There are some deviations from the bounds of the tripartite classification described below, but the grouping captures the essentials of the observed variability.

[20] The first class includes areas with the lowest velocities near the seafloor (<3.4 km s^{-1}) and also the lowest shallow vertical velocity gradients ($<\sim1$ s^{-1}); these are present in the three dip transects (Figure 6a). These features appear in profile K1 east of the Kane OCC termination (volcanic hanging wall terrane, 3 to 10 km model distance), in profile DD4 within the Dante's Domes break-

away zone (-10 to -5 km model distance), and in profile A10 from the Atlantis OCC breakaway zone to the western flank of the Central Dome (-13 to -6 km model distance).

[21] The second class includes areas with intermediate shallow velocities ($3.4-4.2$ km s^{-1}) and generally intermediate velocity gradients ($1-3$ s^{-1}). These are observed beneath the Eve, Abel, and the western half of Cain Dome at Kane OCC (profiles K7 at -15 to -5 km, and K1 at -20 to -7 km), beneath the northern dome of Dante's Domes OCC (profile DD2 at -5 to 7 km), and beneath the
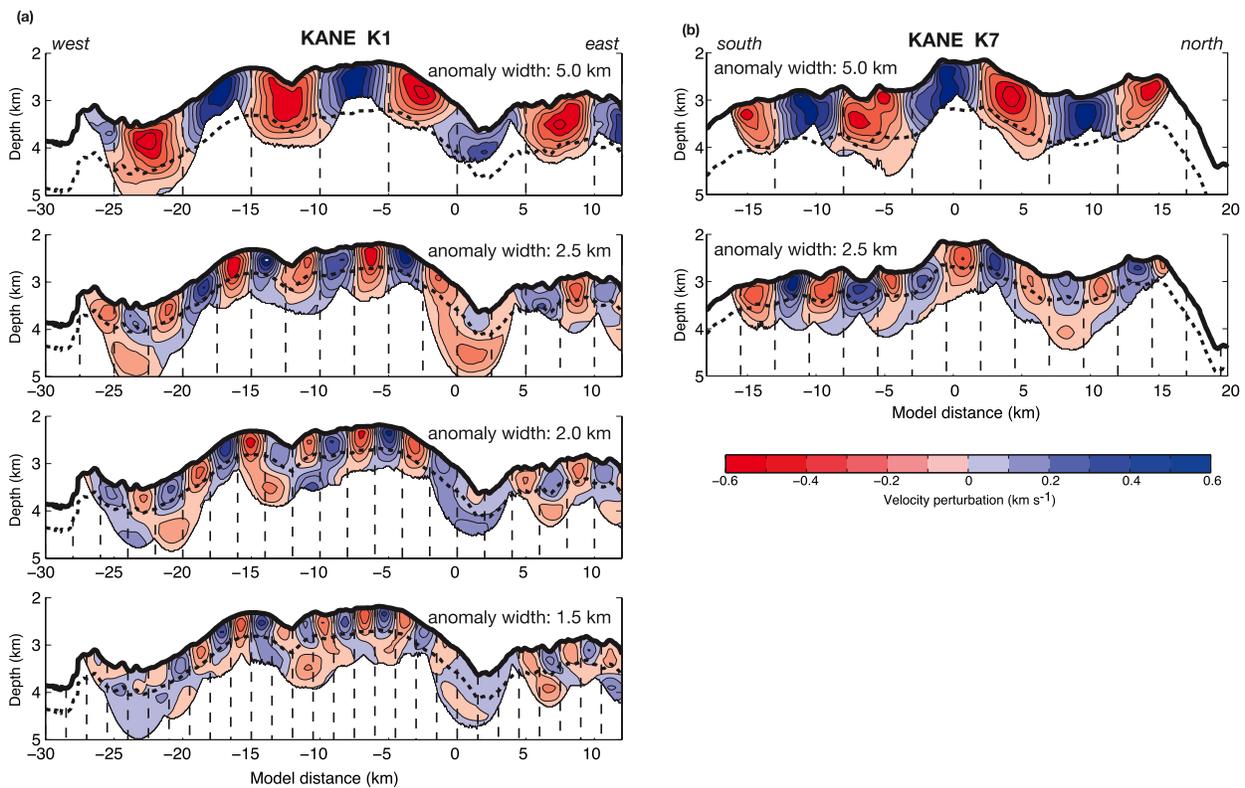
Figure 10. Resolution tests for profiles (a) K1 and (b) K7 of the Kane OCC. Red-blue anomalies show recovered synthetic anomalies. Vertical long-dashed lines locate the alternating positive and negative true anomalies (widths indicated within each panel). Short-dashed lines correspond to a subseafloor depth of 0.5 km, except for the top panels, where it corresponds to 1 km subseafloor depth.

Southern Ridge and north of the Central Dome at Atlantis OCC (profile A4 at −13 to −7 km and 3 to 9 km, respectively).

[22] The third class consists of areas with the highest shallow velocities (>4.2 km s^{-1}) and large shallow velocity gradients (>3 s^{-1}). These characteristics are observed beneath Babel Dome and the eastern half of Cain Dome at Kane OCC (profiles K7 at −5 to 15 km, and K1 at −6 to 0 km), beneath the southern dome at Dante's Domes (profiles DD4 at −4 to13 km, and DD2 at −11 to −6 km), and beneath the eastern part of the Central Dome at Atlantis OCC (profiles A10 at −4 to 2 km, and A4 at −7 to 2 km).

[23] These domains and the transitions between them are best seen when velocities are displayed relative to a laterally invariant, constant vertical-velocity-gradient model that was used as starting model for the tomographic inversions (Figure 4). As shown in Figure 6b, the high-velocity areas are marked by large positive anomalies, the intermediate-velocity areas by both small negative and positive anomalies, and the low-velocity areas by large negative anomalies.

4.2. Comparison With Previous Gravity Studies

[24] Gravity studies have been conducted for a number of OCCs. Most of them have elevated residual mantle Bouguer anomalies, indicative of thin magmatic crust [e.g., *Tucholke et al.*, 1998]. Density models derived from both surface and on-bottom gravity measurements indicate that the cores of OCCs are characterized by relatively high densities consistent with intrusive gabbros and/or partially serpentinized peridotite [*Blackman et al.*, 1998, 2008; *Matsumoto et al.*, 2001; *Nooner et al.*, 2003; *Tucholke et al.*, 2001]. In this section we compare our seismic results with previously published gravity-derived density models from the Atlantis and Dante's Domes OCCs. We base our comparison on the well established positive correlation between density and *P* wave velocity [e.g., *Carlson and Herrick*, 1990] and discuss the similarities and differences between our velocity mod-
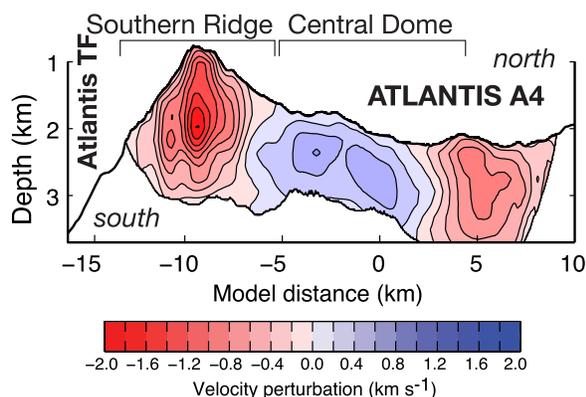
Figure 11. Alternate solution for profile A4 across Atlantis OCC shown as perturbations with respect to the initial one-dimensional velocity model labeled as "A4 alternate initial" in Figure 4; contours are every 0.2 km s^{-1}.

els and the existing density models, but we do not attempt here to interpret the density and velocity models in terms of lithology (complete interpretation of the models is discussed in section 5).

4.2.1. Atlantis

[25] Gravity data from Atlantis OCC indicate the presence of a high-density core (≥2,900 kg m^{-3}) beneath the Central Dome, distributed in a roughly triangular shape in east-west cross-section and bounded to the east and west by lower-density material at shallow levels [*Blackman et al.*, 1998, 2002, 2008; *Nooner et al.*, 2003]. The high-velocity body observed on profile A10 (Figure 6) matches quite well the inferred shape of the high-density core [e.g., see *Blackman et al.*, 2008, Figure 4; *Blackman et al.*, 2002, Figure 16; *Nooner et al.*, 2003, Figure 3]; the west-dipping low- to high-density boundary approximately follows the low- to high-velocity boundary and the bottom of the low-velocity zone on the western side of the Central Dome. Also, the disappearance of the high-velocity body toward the east near 1–2 km model distance coincides with eastward dip of the high-density core toward the axial valley and a transition to lower densities at shallow levels. The independent seismic and density models thus are consistent with one another and mutually support the idea of a core of higher velocity and density basement beneath the eastern part of the Central Dome of Atlantis OCC.

[26] The most recent gravity analysis of Atlantis OCC [*Blackman et al.*, 2008] suggests that the gravity signature of Atlantis OCC might be explained by the same average density beneath the Southern Ridge and Central Dome, with no structural (i.e., density) contrast between them.

This result conflicts with our finding of a fundamentally different seismic structure between the Southern Ridge and Central Dome (profile A4, Figure 6b). Like any tomography inversion, our results depend to some degree on the initial assumptions (i.e., the initial velocity model). Therefore we explored the possibility that our results for profile A4 are influenced by the initial assumptions; for example, might data that sample the Southern Ridge be consistent with a broader range of plausible models than data that sample the Central Dome? We ran an alternate inversion of profile A4, using as a starting velocity model a 1-D structure that is closer to the structure found beneath the Central Dome in our preferred solution (i.e., a seafloor velocity of 4.1 km s^{-1} and vertical velocity gradient of 2.375 s^{-1}, Figure 4). This alternate model (Figure 11) converges to a traveltime misfit of $\chi^2 = 1.2$ in 4 iterations. The results show the same general pattern as the preferred solution, i.e., high velocities beneath the Central Dome that are bounded to the north and south by significantly lower velocities. Note that compared to Figure 6b, Figure 11 shows larger-amplitude negative anomalies and smaller-amplitude positive anomalies because the alternate starting model had higher velocity than in the preferred solutions. This test demonstrates that the contrasting seismic character between the Southern Ridge and Central Dome is required by the data and is not biased by the starting model chosen.

[27] To reconcile our velocity model for profile A4 with the gravity data, we are left with the possibility that the model proposed by *Blackman et al.* [2008] may be simplistic in its use of a single density to define the core of the Southern Ridge. If, for example, the low velocities observed beneath the Southern Ridge overlie high velocities (i.e., unaltered peridotitic mantle) deeper than ~1500–2000 m below seafloor, lithosphere beneath the Southern Ridge could still have integrated density similar to that of the Central Dome, despite having different structure (a layered structure or a vertical density gradient) that would be consistent with our seismic results.

4.2.2. Dante's Domes

[28] Density modeling across Dante's Domes OCC has been done using both surface and on-bottom gravity measurements [*Tucholke et al.*, 2001]. The modeled density structure across this OCC from breakaway to termination agrees very well with our seismic results. The eastern limit of the high-velocity body near the breakaway zone (−4 km

model distance in profile DD4, Figure 6) coincides with a density boundary between lower-density material to the east and the higher-density core of the OCC [see *Tucholke et al.*, 2001, Figure 9]. The density model also includes a high-density (i.e., unaltered mantle) body located at ~4.5 km beneath the central part of the OCC that shoals to just ~1.5 km near the breakaway. Unfortunately our data do not image deeply enough to model this boundary, but future seismic experiments with a larger source-receiver aperture could easily test the deeper parts of the density model.

5. Correlation of Seismic Structure and Lithology

[29] Extensive geological sampling has been conducted at Atlantis and Kane OCC, and this allows us to correlate the main seismic characteristics that we observe with predominant lithologies. Our interpretation is also guided by considering the seismic results within their tectonic context and visualizing them together with the three-dimensional surrounding topography (Figure 12 and auxiliary material[1] Animations S1 and S2).

[30] At Atlantis OCC, velocities on profiles A4 and A10 closest to Hole U1309D at the Central Dome agree quite closely with the compressional velocities measured in situ within the hole [*Blackman et al.*, 2006] (Figure 4). We therefore argue that gabbros are the dominant, although not necessarily exclusive, lithology forming the high-velocity body beneath the Central Dome. There is strikingly similar velocity structure in the other two OCCs near their terminations (Figures 6 and 12), and we interpret all these high-velocity zones as representing predominantly gabbros. At Kane OCC, this is consistent with samples obtained from Babel Dome [*Dick et al.*, 2008] and the southern wall of the Kane TF [*Auzende et al.*, 1994] (Figures 6 and 12), where gabbro appears to be the primary lithology. Our interpretation is also consistent with seismic and drilling results from ODP Hole 735B in the Atlantis Bank OCC on the Southwest Indian Ridge; average seismic velocities of 6 km s^{-1} [*Muller et al.*, 1997] are found there in the upper crust where drilling recovered ~1500 m of gabbroic rocks [*Dick et al.*, 2000].

[31] Intermediate velocities beneath the Southern Ridge at Atlantis OCC on the MAR correlate with massive outcrops of serpentinized peridotite that

are exposed along the southern margin of the ridge [*Blackman et al.*, 2002; *Karson et al.*, 2006] (Figures 6 and 12). In this area velocities of 6 km s^{-1} are not observed until ~1500 m below the seafloor (Figures 4 and 6); this indicates large degrees of serpentinization (>80%) [*Miller and Christensen*, 1997] from the seafloor to at least those depths, in agreement with samples from the south flank of the Southern Ridge [*Boschi et al.*, 2006]. Similar velocity structure occurs between Abel and Cain Domes in the Kane OCC, where East Fault exposes massive outcrops of serpentinized peridotite [*Dick et al.*, 2008]. The consistency of this correlation indicates that serpentinized peridotites are predominant beneath the smooth, corrugated fault surface at Abel Dome and the western side of Cain Dome (Figures 6 and 12). This lithology-velocity correlation also suggests that the intermediate-velocity area beneath the northern dome at Dante's Domes OCC (profile DD2) may be predominantly serpentinized peridotite. A similar correlation may apply at Atlantis OCC north of the Central Dome at (profile A4), where gravity modeling indicates low-density basement rocks [*Blackman et al.*, 2002, 2008]. However, seafloor morphology shows that volcanic rocks form at least the upper part of the basement section there [*Blackman et al.*, 2002, 2008].

[32] Areas with the lowest velocities most likely consist of volcanics and sheeted dikes, at least in their upper parts. These velocity characteristics appear in the hanging walls of the detachment faults, as best seen on profile K1 where hummocky seafloor morphology clearly shows the presence of dominant volcanics (Figure 12; see also auxiliary material Animations S1 and S2). They also occur near the fault breakaways (Figure 6) where, for example at Dante's Domes OCC, in situ pillow basalts have been observed in submersible dives [*Tucholke et al.*, 2001].

[33] Our lithologic interpretation of the velocity models indicates that there is large variability in the distribution of gabbros and serpentinized peridotites within the three OCCs studied here. At Atlantis OCC the Central Dome is mostly gabbroic from the summit of the corrugated surface to near the termination. This gabbroic core is bounded to the south (and perhaps to the north) by predominantly ultramafic lithosphere (Figures 6b and 12). Our seismic results clearly confirm a distinct lithological contrast between the mafic Central Dome and the ultramafic Southern Ridge, as previously
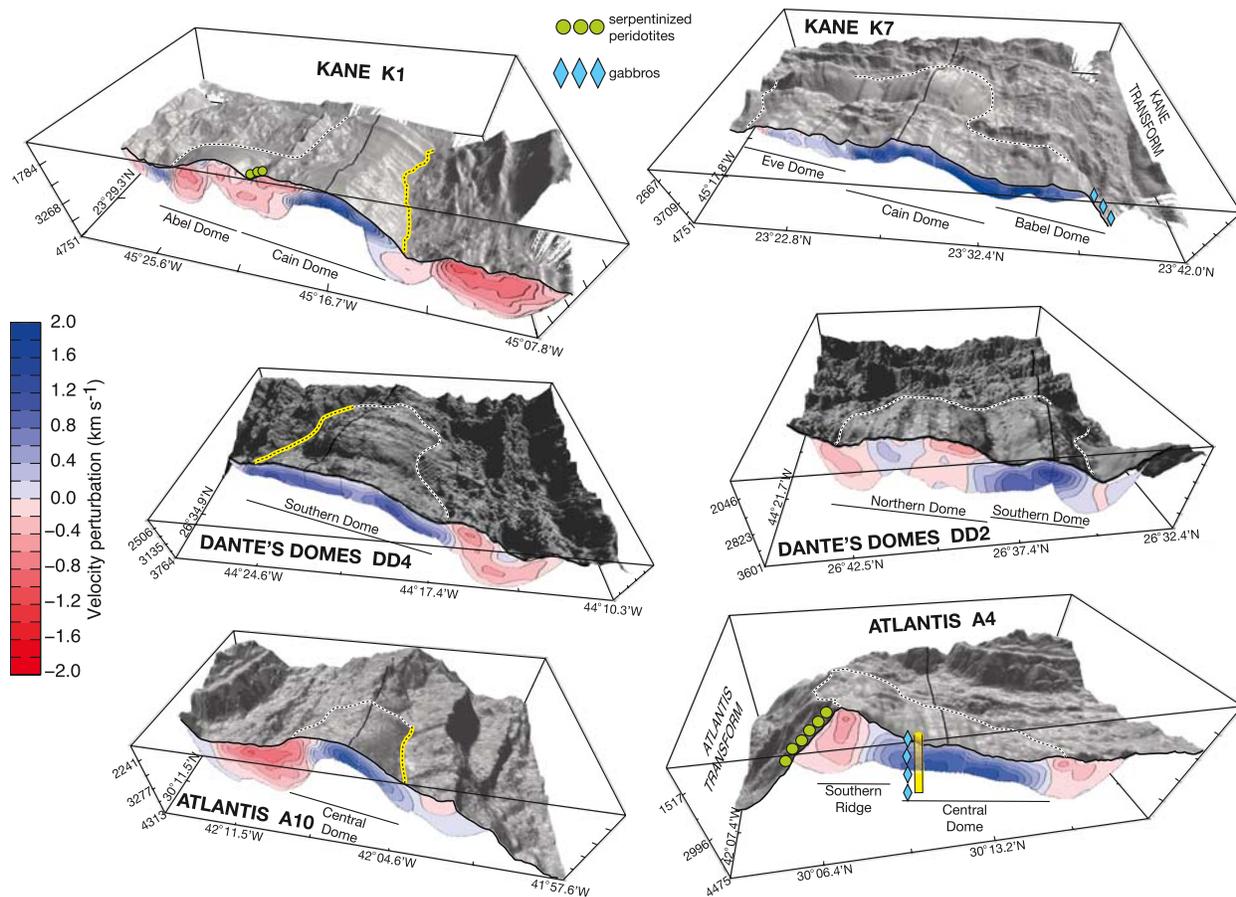
Figure 12. Three-dimensional renditions of seafloor topography (shaded gray) with intersecting vertical sections of the velocity profiles (red-blue images showing velocity perturbations as in Figure 6b, contoured every 0.2 km s^{-1}). Left panels show dip sections, and right panels show strike sections. Blue and red areas indicate velocities faster and slower than the reference model, respectively. Dashed lines on the seafloor topography indicate the limits of dominantly smooth, corrugated detachment surfaces; yellow segments show detachment terminations. Solid black lines draped on the seafloor locate the orthogonal seismic profiles at each OCC. Colored dots and diamonds are in situ lithologies as in Figure 6. Vertical yellow bar in profile A4 locates IODP Hole U1309D. Primary morphological features are labeled. Horizontal axes are latitude and longitude, and vertical axes show depth below sea level in meters.

suggested on the basis of geological samples [*Karson et al.*, 2006].

[34] At the Kane OCC, the velocity structure of Cain Dome is very similar to the Atlantis Central Dome, with a gabbroic core forming the eastern part of the dome, from the summit to near the termination (Figures 6 and 12). Farther north, the velocity structure of Babel Dome also indicates a gabbroic composition, but to the south Eve Dome has an intermediate structure that may correspond to a mixture of mafic and ultramafic rocks (Figures 6 and 12). In contrast, the western side of Cain Dome and the older Abel Dome are interpreted to be predominantly ultramafic.

[35] At Dante's Domes OCC the southern dome shows similarities to the Central Dome of Atlantis OCC and Cain Dome at Kane OCC, although a dominantly gabbroic composition appears to extend nearly continuously from near the breakaway to the termination (Figures 6 and 12). The northern dome, however, has velocity structure more like that of the Southern Ridge at Atlantis OCC and Abel Dome at Kane OCC (Figure 12), suggesting a predominance of serpentinites.

6. Discussion

6.1. Distinguishing Between Gabbros and Serpentinized Peridotites on the Basis of Their *P* Wave Velocity

[36] Laboratory measurements of *P* wave velocity (V_P) in hand-samples of oceanic gabbros and serpentinized peridotites at appropriate confining pressures indicate that V_P ranges between 6.7 and

7.3 km s^{-1} for gabbros, and between 4.8 and 8.0 km s^{-1} for fully serpentinized and fresh peridotites, respectively [e.g., *Miller and Christensen*, 1997]. *P* wave velocity fields for both lithologies overlap when the degree of serpentinization of the peridotites is ∼20–40%. For this reason there is inherent ambiguity when interpreting as gabbros or serpentinized peridotites seismic velocities measured by remote methods (e.g., seismic refraction methods) in the 6.7–7.3 km s^{-1} range, in the absence of other independent constraints such as direct sampling, gravity data, or V_P/V_S ratio. In contrast, highly serpentinized peridotites (>40%) should be distinguishable from gabbroic rocks on the basis of their V_P, but they may become harder to differentiate from basaltic rocks such as extrusive lavas and dikes owing to their lower velocity.

[37] A key result from our study is that we can make such a distinction because (1) we base our interpretation on correlation to in situ samples and characteristic seafloor morphology, which allows us to distinguish volcanic settings from serpentinized peridotite exposures, and (2) the sampled serpentinized peridotites show high degrees of serpentinization (>70% [*Boschi et al.*, 2006]), making them distinguishable from gabbros. The high-velocity regions we interpret as predominantly gabbros could also be interpreted as predominantly peridotites with moderate degree of serpentinization (20–40%); however, the constraints provided by the IODP Hole 1309D results make this possibility unlikely.

[38] It is important to note that seismic velocities derived from remote methods such as those used in this study tend to be lower than velocities measured in laboratory samples in part because data from the seismic experiments are sensitive to fractures occurring at scales larger than the laboratory samples. This could explain why we measure velocities lower than 6 km s^{-1} at the location of IODP Hole 1309D (Figure 4), significantly lower than the 6.7–7.3 km s^{-1} expected for intact gabbro samples [*Miller and Christensen*, 1997], or velocities lower than 4.8 km s^{-1} (the expected value for fully serpentinized peridotite) in the upper 1 km of the Southern Ridge of Atlantis OCC (Figure 4).

6.2. Comparison of Velocity Model With Seismic Reflectivity Beneath the Atlantis OCC

[39] Some of the data used in this study were used previously to image subseafloor reflections across the Atlantis OCC [*Canales et al.*, 2004]. These authors reported the presence of a shallow reflection, termed *D*, beneath parts of the core complex. Similar shallow reflections recently have been reported at other oceanic core complexes [*Ohara et al.*, 2007b]. The *D* reflection was best imaged along profile A10 (profile Meg-10 of *Canales et al.* [2004]), and was interpreted as a possible older detachment fault. IODP Hole U1309D cored through this reflection and recovered gabbros with no evidence of a major fault interface; thus the results do not support the interpretation of a secondary detachment. Figure 13 compares our tomography results along profile A10 with the corresponding reflection image of *Canales et al.* [2004], and it shows that the *D* reflection approximately follows the ∼5.5 km s^{-1} isovelocity contour, roughly marking the transition from low to high velocities from west to east across the Central Dome of Atlantis OCC. We suggest that the *D* reflection at this location correlates with a rapid increase in seismic velocity associated with the top of the gabbroic core forming the eastern half of the Central Dome. In this and adjacent areas where the gabbroic core is probably close to, or exposed at, the seafloor (e.g., at the location of IODP Hole U1309D), the *D* reflection may correspond to velocity change related to a shallow fracturing or alteration front in the gabbro.

6.3. Lithospheric Structure During Early Stages of the OCC Formation

[40] Differences among the three OCCs are emphasized in the velocity structure of the lithosphere exhumed shortly after fault breakaways (Figures 6 and 12). The Kane detachment fault initially cut through a shallow section of probable gabbro (Figure 6b) and shortly thereafter was exhuming mantle for about 0.5 Ma. This indicates that early development of the Kane OCC was in a magma-limited environment. In contrast, the detachment at the southern dome of Dante's Domes OCC quickly exhumed a gabbro section that continued to fault termination, while at Atlantis OCC the detachment appears to have transected a thick, low-velocity, volcanic (and possibly dike?) section before gabbros were finally exhumed.

6.4. Large Gabbroic Intrusions and OCCs

[41] The major common characteristic of each of the three OCCs is the high-velocity body between the OCC summit and the termination, which we interpret as a gabbroic core (Figures 6 and 12).
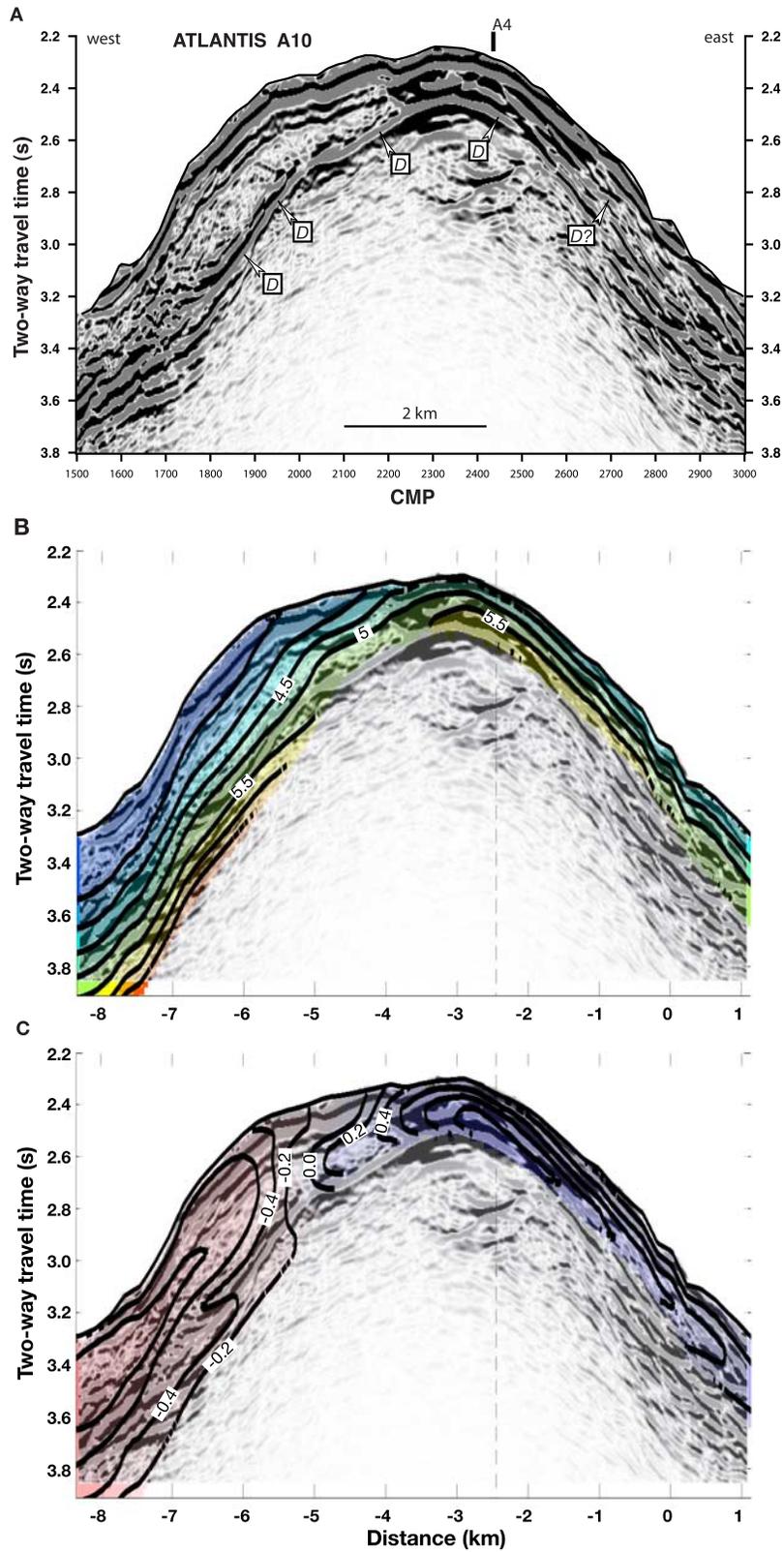
Figure 13

Consistent with this apparent increased melt supply with time, all three OCCs show reduced residual mantle Bouguer gravity anomalies toward their terminations [*Nooner et al.*, 2003; *Tucholke et al.*, 1998, 2001]. It has been recently hypothesized that large gabbroic intrusions may be required to localize strain and develop oceanic detachment faults [*Ildefonse et al.*, 2007] owing to the rheological differences between gabbro and serpentinized peridotite [*Escartín et al.*, 2001], and that the detachments nucleate along the irregular brittle-plastic transition around the gabbroic intrusions to form observed corrugations [*Tucholke et al.*, 2008]. Our findings appear to support these ideas, although there are some possible inconsistencies. Along the Atlantis and Dante's Domes dip profiles, the fault surface from breakaway to the first downdip gabbro body ranges in distance from ∼3–12 km; this would mean that the fault initially broke to depths shallower than ∼11 km (assuming fault dip between 45° and 70°), which is not unreasonable [*deMartin et al.*, 2007]. A similar fault may have nucleated on the small, shallow body of probable gabbro near the breakaway of the Kane OCC (profile K1, Figure 6b). However, if the Kane detachment instead nucleated above the gabbros in Cain dome, the fault would have extended downdip ∼20 km and reached a depth of 14–18 km, which seems unlikely.

[42] Similar distributions of apparent gabbro bodies near detachment terminations can be inferred at Godzilla Mullion in the Parece Vela Basin in the Philippine Sea, which is the largest OCC found to date and occupies a ∼130-km-long, ∼60-km-wide corridor of corrugated seafloor between breakaway and termination [*Ohara et al.*, 2001]. (Recent seismic results from other OCCs in the Parece Vela Basin [*Ohara et al.*, 2007b] are more difficult to compare to our results because those profiles are oblique to the paleo-spreading direction and corrugations, and they do not always cross the main domes of the OCCs.) An ocean bottom seismometer seismic refraction profile in the dip direction over Godzilla Mullion [*Ohara et al.*, 2007a] indicates that the ∼40-km-long section of the OCC near the termination is characterized by unusually high seismic velocities reaching 6 km s^{-1} as shallow as ∼500 m below seafloor, while the older,

∼90-km-long part of the OCC has lower seismic velocities (6 km s^{-1} are not reached until ∼2 km below seafloor). This pattern of relatively high seismic velocities near the termination is very similar to results along our dip profiles (particularly along profile K1), but it occurs at much larger scale. If the high-velocity body at Godzilla Mullion was a gabbro core on which the detachment fault nucleated, it would require that the fault broke to an unrealistic depth of >60 km (following the same reasoning as above), which would argue against the model of *Ildefonse et al.* [2007]. However, it must be noted that the Godzilla Mullion seismic dip line is only a narrow sample of velocity structure within the ∼60-km wide OCC, and there could be high-velocity gabbro bodies in lateral, along-strike directions near the breakaway that presently are undetected.

[43] The strike lines at Dante's Domes OCC and Atlantic OCC (Figure 6b) show low velocities beneath the northern dome at Dante's Domes and beneath the Southern Ridge at Atlantis OCC. This observation also seems to argue against the model of *Ildefonse et al.* [2007], which predicts that the Southern Ridge of Atlantis OCC is of the same nature/origin as the Central Dome, with a gabbroic core surrounded by a thin layer of serpentinized peridotite. However, it is possible that gabbro bodies are present closer to the breakaways, and they have not been detected in our seismic experiments owing to the limited data coverage near breakaways. Thus, in order fully to understand the extent to which detachments may nucleate on deep-seated gabbro bodies, it will be necessary to obtain strike-line velocity data in the critical zone less than ∼10 km from detachment breakaways.

[44] In contrast to the fault nucleation hypothesis discussed above, an alternate interpretation for the gabbro cores near the terminations of the Kane, Dante's Domes, and Atlantis OCCs is that they are an independent, late-stage phenomenon. The enhanced magmatism might occur in either of two ways. First, it could be part of a natural magmatic cycle controlled by the fertility or dynamics of melt flow in the upwelling mantle. Such cycles have been documented to occur in the flanks of the MAR at periods ranging from ∼0.4–0.8 Ma [*Canales et al.*, 2000] to ∼2–3 Ma [*Sempéré et*

Figure 13. (a) Multichannel seismic reflection dip profile A10 across the top of the Central Dome of Atlantis OCC (profile Meg-10 in figure from *Canales et al.* [2004]) showing the shallow *D* reflection. The intersection of orthogonal profile A4 is indicated. (b) The same seismic section overlaid with the velocity tomography model of this study (labeled in km s^{-1}), lightly colored (color scale as in Figure 6a) and converted to two-way traveltime. (c) Seismic reflection profile as above but overlaid with velocity perturbation in km s^{-1} relative to the starting model, as in Figure 6b.

al., 1995; *Tucholke et al.*, 1997]. Alternatively, it might be the result of decompression melting in the exhuming footwall. Recent numerical models that explore the conditions that lead to the formation and growth of long-lived oceanic detachment faults predict that axial lithospheric thermal structure can become highly asymmetrical owing to the advection of hot material into the footwall of the fault [*Tucholke et al.*, 2008]. Such asymmetrical thermal structure might eventually stimulate melting in the exhuming footwall if the rising mantle is sufficiently fertile, and it would thus result in emplacement of the gabbro bodies. Lateral variations in composition and fertility of the mantle could modulate melt production and thus account for the broader spatial heterogeneity of the gabbros.

[45] Irrespective of the cause of the increased melt supply, a possible consequence is that this increase could lead to abandonment of the detachment fault [*Buck et al.*, 2005; *Tucholke et al.*, 1998, 2008]. Heat introduced by the flow and crystallization of melt could weaken the lithosphere at the ridge axis to the point that a new fault or set of faults would form there and take up plate separation formerly accommodated by the detachment.

7. Concluding Remarks

[46] In this study we have shown that seismic reflection/refraction data acquired with a large-offset hydrophone streamer is a powerful tool for determining the uppermost seismic structure of the oceanic lithosphere where it is exposed in relatively shallow OCCs. Such seismic studies, when integrated with good sample and morphological constraints, can map with a high degree of confidence the lateral variations in the dominant composition of the oceanic lithosphere at scales of a few kilometers.

[47] Our seismic tomography results indicate that gabbros occur in large bodies (tens to >100 km^2) and have a heterogeneous distribution within shallow lithosphere that is exhumed by long-lived oceanic detachment faults. This observation suggests that large-scale melt flux from the mantle is irregularly distributed within spreading segments and is not necessarily focused at segment centers as has been previously postulated [*Whitehead et al.*, 1984]. A similar conclusion has been reached for the Kane OCC on the basis of extensive rock sampling [*Dick et al.*, 2008].

[48] The tomography profiles also suggest widespread distribution of serpentinized peridotite with-

in the OCCs. Such serpentinization can sustain hydrothermal circulation driven by exothermic reactions, as has been proposed for the Lost City field on the Southern Ridge of Atlantis OCC [*Früh-Green et al.*, 2003]. Thus, despite the common occurrence of large gabbroic cores, OCCs, appear to have significant potential to host serpentinite-based hydrothermal systems. Seismic studies like those described here can be an important tool in the search for new non-magmatic hydrothermal ecosystems within OCCs.

[49] We consistently observe high-velocity gabbros toward the terminations of the OCCs studied. These might be emplaced either because of natural variability in the magmatic cycle or because of decompression melting within the rapidly exhuming footwall [*Tucholke et al.*, 2008], but in either case the newly introduced heat may contribute to formation of new faults and abandonment of the detachment. If decompression melting is significant, then large parts of OCCs, particularly those close to the termination, may be affected by melting, flow, and emplacement of magma that overprints the pre-existing geological record of these processes. Although this kind of overprinting is to be expected in any ocean crust affected by the flow of melt, the process may well be exaggerated in the case where rapid exhumation is caused by detachment faulting.

[50] If the gabbroic cores interpreted in our seismic profiles are an integral component of detachment faulting and OCC formation, then large oceanic detachment faults are non-conservative because new material is added to the footwall during exhumation. For this reason, *Dick et al.* [2008] have proposed that such faults should be termed ''plutonic growth faults.'' This hypothesis will need to be tested by thermal and mechanical numerical models such as those of *Buck et al.* [2005] and *Tucholke et al.* [2008].

[51] Finally, we note that our study is limited to the uppermost lithosphere, and it leaves open questions about the deeper geometry of the gabbroic cores, along-strike variability near breakaways, and depth extent of serpentinization. These questions must be addressed with both deeper and more complete geophysical imaging and by drilling.

Acknowledgments

tific party of R/V *Maurice Ewing* Cruise 0102. This study benefited from discussions with H. Dick, J. Escartín, and H. Schouten and from reviews by D. Blackman and an anonymous reviewer. We thank H. Dick and M. A. Tivey for sharing data on Kane OCC geological samples with us during the course of our study. The software Focus by Paradigm™ was used in the seismic data processing.

References

Auzende, J.-M., M. Cannat, P. Gente, J.-P. Henriet, T. Juteau, J. A. Karson, Y. Lagabrielle, C. Mével, and M. A. Tivey (1994), Observation of sections of oceanic crust and mantle cropping out on the southern wall of Kane FZ (N. Atlantic), *Terra Nova*, *6*, 143–148, doi:10.1111/j.1365-3121.1994.tb00647.x.

Blackman, D. K., J. R. Cann, B. Janssen, and D. K. Smith (1998), Origin of extensional core complexes: Evidence from the Mid-Atlantic Ridge at Atlantis Fracture Zone, *J. Geophys. Res.*, *103*(B9), 21,315–21,333, doi:10.1029/98JB01756.

Blackman, D. K., et al. (2002), Geology of the Atlantis Massif (Mid-Atlantic Ridge, 30°N): Implications for the evolution of an ultramafic oceanic core complex, *Mar. Geophys. Res.*, *23*, 443–469, doi:10.1023/B:MARI.0000018232.14085.75.

Blackman, D. K., B. Ildefonse, B. E. John, Y. Ohara, D. J. Miller, C. J. MacLeod, and Expedition 304/305 Scientists (2006), Oceanic core complex formation, Atlantis Massif, in *Proc. Integrated Ocean Drill. Program, 304/305*, doi:10.2204/iodp.proc.304305.302006.

Blackman, D. K., G. D. Karner, and R. C. Searle (2008), Three-dimensional structure of oceanic core complexes: Effects on gravity signature and ridge flank morphology, Mid-Atlantic Ridge, 30°N, *Geochem. Geophys. Geosyst.*, *9*, Q06007, doi:10.1029/2008GC001951.

Boschi, C., G. L. Früh-Green, A. Delacour, J. A. Karson, and D. S. Kelley (2006), Mass transfer and fluid flow during detachment faulting and development of an oceanic core complex, Atlantis Massif (MAR 30°N), *Geochem. Geophys. Geosyst.*, *7*, Q01004, doi:10.1029/2005GC001074.

Buck, W. R., L. L. Lavier, and A. N. B. Poliakov (2005), Modes of faulting at mid-ocean ridges, *Nature*, *434*, 719–723, doi:10.1038/nature03358.

Canales, J. P., J. A. Collins, J. Escartín, and R. S. Detrick (2000), Seismic structure across the rift valley of the Mid-Atlantic Ridge at 23°20′ (MARK area): Implications for crustal accretion processes at slow spreading ridges, *J. Geophys. Res.*, *105*(B12), 28,411–28,425, doi:10.1029/2000JB900301.

Canales, J. P., B. E. Tucholke, and J. A. Collins (2004), Seismic reflection imaging of an oceanic detachment fault: Atlantis megamullion (Mid-Atlantic Ridge, 30°10′N), *Earth Planet. Sci. Lett.*, *222*, 543–560, doi:10.1016/j.epsl.2004.02.023.

Cann, J. R., D. K. Blackman, D. K. Smith, E. McAllister, B. Janssen, S. Mello, E. Avgerinos, A. R. Pascoe, and J. Escartín (1997), Corrugated slip surfaces formed at ridge-transform intersections on the Mid-Atlantic Ridge, *Nature*, *385*, 329–332, doi:10.1038/385329a0.

Cannat, M., V. Mendel, E. Ruellan, K. Okino, J. Escartín, V. Combier, and M. Baala (2006), Modes of seafloor generation at a melt-poor ultraslow-spreading ridge, *Geology*, *34*, 605–608, doi:10.1130/G22486.1.

Carlson, R. L., and C. N. Herrick (1990), Densities and porosities in the oceanic crust and their variations with depth

and age, *J. Geophys. Res.*, *95*, 9153–9170, doi:10.1029/JB095iB06p09153.

deMartin, B. J., R. Reves-Sohn, J. P. Canales, and S. E. Humphris (2007), Kinematics and geometry of active detachment faulting beneath the Trans-Atlantic Geotraverse (TAG) hydrothermal field on the Mid-Atlantic Ridge, *Geology*, *35*, 711–714, doi:10.1130/G23718A.1.

DeMets, C., R. G. Gordon, D. F. Argus, and S. Stein (1990), Current plate motions, *Geophys. J. Int.*, *101*, 425–478, doi:10.1111/j.1365-246X.1990.tb06579.x.

Dick, H. J. B., et al. (2000), A long in situ section of the lower ocean crust: Results of ODP Leg 176 drilling at the Southwest Indian ridge, *Earth Planet. Sci. Lett.*, *179*, 31–51, doi:10.1016/S0012-821X(00)00102-3.

Dick, H. J. B., M. A. Tivey, and B. E. Tucholke (2008), Plutonic foundation of a slow-spreading ridge segment: Oceanic core complex at Kane Megamullion, 23°30′N, 45°20′W, *Geochem. Geophys. Geosyst.*, *9*, Q05014, doi:10.1029/2007GC001645.

Escartín, J., G. Hirth, and B. Evans (2001), Strength of slightly serpentinized peridotites: Implications for the tectonics of oceanic lithosphere, *Geology*, *29*, 1023–1026, doi:10.1130/0091-7613(2001)029<1023:SOSSPI>2.0.CO;2.

Escartín, J., C. Mével, C. J. MacLeod, and A. M. McCaig (2003), Constraints on deformation conditions and the origin of oceanic detachments: The Mid-Atlantic Ridge core complex at 15°45′N, *Geochem. Geophys. Geosyst.*, *4*(8), 1067, doi:10.1029/2002GC000472.

Früh-Green, G. L., D. S. Kelley, S. M. Bernasconi, J. A. Karson, K. A. Ludwig, D. A. Butterfield, C. Boschi, and G. Proskurowski (2003), 30,000 years of hydrothermal activity at the Lost City vent field, *Science*, *301*, 495–498, doi:10.1126/science.1085582.

Harding, A. J., G. M. Kent, D. K. Blackman, S. Singh, and J. P. Canales (2007), A new method for MCS refraction data analysis of the uppermost section at a Mid-Atlantic Ridge core complex, *Eos Trans. AGU*, *88*(52), Fall Meet. Suppl., Abstract S12A-03.

Ildefonse, B., D. K. Blackman, B. E. John, Y. Ohara, D. J. Miller, C. J. MacLeod, and Integrated Ocean Drilling Program Expeditions 304/305 Science Party (2007), Oceanic core complexes and crustal accretion at slow-spreading ridges, *Geology*, *35*, 623–626, doi:10.1130/G23531A.1.

Karson, J. A., G. L. Früh-Green, D. S. Kelley, E. A. Williams, D. R. Yoerger, and M. Jakuba (2006), Detachment shear zone of the Atlantis Massif core complex, Mid-Atlantic Ridge, 30°N, *Geochem. Geophys. Geosyst.*, *7*, Q06016, doi:10.1029/2005GC001109.

Kelemen, P. B., E. Kikawa, D. J. Miller, and the Shipboard Scientific Party (2004), *Proceedings of the Ocean Drilling Program, Initial Reports*, vol. 209, Ocean Drill. Program, College Station, Tex., doi:10.2973/odp.proc.ir.2209.2004.

Kelley, D. S., et al. (2001), An off-axis hydrothermal vent field near the Mid-Atlantic Ridge at 30°N, *Nature*, *412*, 145–149, doi:10.1038/35084000.

MacLeod, C. J., et al. (2002), Direct geological evidence for oceanic detachment faulting: The Mid-Atlantic Ridge, 15°45′N, *Geology*, *30*, 879–882, doi:10.1130/0091-7613(2002)030<0879:DGEFOD>2.0.CO;2.

Matsumoto, T., A. Hosford, and H. J. B. Dick (2001), Gravity signal of the mantle exposure on the Atlantis Bank and the Atlantis-II fracture zone, Southwest Indian ridge (abstract), paper presented at EGS XXVI General Assembly, Eur. Geophys. Soc., Nice, France.

Miller, D. J., and N. I. Christensen (1997), Seismic velocities of lower crustal and upper mantle rocks from the slow

spreading Mid-Atlantic Ridge, south of the Kane transform zone (MARK), *Proc. Ocean Drill. Program Sci. Results*, *153*, 437–454.

Muller, M. R., C. J. Robinson, T. A. Minshull, R. S. White, and M. J. Bickle (1997), Thin crust beneath ocean drilling program borehole 735B at the Southwest Indian Ridge?, *Earth Planet. Sci. Lett.*, *148*, 93–107, doi:10.1016/S0012-821X(97)00030-7.

Nooner, S. L., G. S. Sasagawa, D. K. Blackman, and M. A. Zumberge (2003), Structure of oceanic core complexes: Constraints from seafloor gravity measurements made at the Atlantis Massif, *Geophys. Res. Lett.*, *30*(8), 1446, doi:10.1029/2003GL017126.

Ohara, Y., T. Yoshida, and S. Kasuga (2001), Giant megamullion in the Parece Vela Backarc basin, *Mar. Geophys. Res.*, *22*, 47–61, doi:10.1023/A:1004818225642.

Ohara, Y., Y. Ohara, K. Okino, J. E. Snow, and Science Party (2007a), IODP site survey for drilling Godzilla Mullion: Preliminary report of R/V Hakuho KH07-2 Leg 2 & 4 cruise, *Eos Trans. AGU*, *88*(52), Fall Meet. Suppl., Abstract T53B-1314.

Ohara, Y., K. Okino, and J. Kasahara (2007b), Seismic study on oceanic core complexes in the Parece Vela back-arc basin, *Island Arc*, *16*, 348–360, doi:10.1111/j.1440-1738.2007.00591.x.

Okino, K., K. Matsuda, D. M. Christie, Y. Nogi, and K. Koizumi (2004), Development of oceanic detachment and asymmetric spreading at the Australian-Antarctic Discordance, *Geochem. Geophys. Geosyst.*, *5*, Q12012, doi:10.1029/2004GC000793.

Reston, T. J., W. Weinrebe, I. Grevemeyer, E. R. Flueh, N. C. Mitchell, L. Kirstein, C. Kopp, and H. Kopp (2002), A rifted inside corner massif on the Mid-Atlantic Ridge at 5°S, *Earth Planet. Sci. Lett.*, *200*, 255–269, doi:10.1016/S0012-821X(02)00636-2.

Searle, R. C., M. Cannat, K. Fujioka, C. Mével, H. Fujimoto, A. Bralee, and L. Parson (2003), FUJI Dome: A large detachment fault near 64°E on the very slow-spreading southwest Indian Ridge, *Geochem. Geophys. Geosyst.*, *4*(8), 9105, doi:10.1029/2003GC000519.

Sempéré, J.-C., et al. (1995), The Mid-Atlantic Ridge between 29°N and 31°30′N in the last 10 Ma, *Earth Planet. Sci. Lett.*, *130*, 45–55, doi:10.1016/0012-821X(94)00259-2.

Shipp, R. M., and S. C. Singh (2002), Two-dimensional full wavefield inversion of wide-aperture marine seismic streamer data, *Geophys. J. Int.*, *151*, 325–344, doi:10.1046/j.1365-246X.2002.01645.x.

Smith, D. K., J. R. Cann, and J. Escartín (2006), Widespread active detachment faulting and core complex formation near 13°N on the Mid-Atlantic Ridge, *Nature*, *442*, 440–443, doi:10.1038/nature04950.

Tucholke, B. E., and J. Lin (1994), A geological model for the structure of ridge segments in slow spreading ocean crust, *J. Geophys. Res.*, *99*, 11,937–11,958, doi:10.1029/94JB00338.

Tucholke, B. E., J. Lin, and M. C. Kleinrock (1996), Mullions, megamullions, and metamorphic core complexes on the Mid-Atlantic Ridge, *Eos Trans. AGU*, *77*(46), Fall Meet. Suppl., F724.

Tucholke, B. E., J. Lin, M. C. Kleinrock, M. A. Tivey, T. B. Reed, J. A. Goff, and G. E. Jaroslow (1997), Segmentation and crustal structure of the western Mid-Atlantic Ridge flank, 25°25′-27°10′ and 0-29 m.y., *J. Geophys. Res.*, *102*, 10,203–10,223, doi:10.1029/96JB03896.

Tucholke, B. E., J. Lin, and M. C. Kleinrock (1998), Megamullions and mullion structure defining oceanic metamorphic core complexes on the Mid-Atlantic Ridge, *J. Geophys. Res.*, *103*, 9857–9866, doi:10.1029/98JB00167.

Tucholke, B. E., K. Fujioka, T. Ishihara, G. Hirth, and M. Kinoshita (2001), Submersible study of an oceanic megamullion in the central North Atlantic, *J. Geophys. Res.*, *106*, 16,145–16,161, doi:10.1029/2001JB000373.

Tucholke, B. E., M. D. Behn, R. Buck, and J. Lin (2008), The role of melt supply in oceanic detachment faulting and formation of megamullions, *Geology*, *36*, 455–458, doi:10.1130/G24639A.1.

Whitehead, J. A., H. J. B. Dick, and H. Schouten (1984), A mechanism for magmatic accretion under spreading centers, *Nature*, *312*, 146–148, doi:10.1038/312146a0.

Williams, C. M., M. A. Tivey, and M. D. Behn (2006), The magnetic structure of Kane megamullion: Results from marine magnetic anomalies, paleomagnetic data and thermal modeling, *Eos Trans. AGU*, *87*(52), Fall Meet. Suppl., Abstract T42A-03.

Xu, M., J. P. Canales, B. E. Tucholke, and D. L. Dubois (2007), Shallow seismic structure of the Kane core complex, Mid-Atlantic Ridge 23°30′N, *Eos Trans. AGU*, *88*(52), Fall Meet. Suppl., Abstract T53B-1304.

Yilmaz, Ö. (1987), *Seismic Data Processing*, *Invest. Geophys.*, vol. 2, 526 pp., Soc. of Explor. Geophys., Tulsa, Okla.

Zelt, C. A., and P. J. Barton (1998), Three-dimensional seismic refraction tomography: A comparison of two methods applied to data from the Faeroe Basin, *J. Geophys. Res.*, *103*, 7187–7210, doi:10.1029/97JB03536.

Zelt, C. A., and D. A. Forsyth (1994), Modeling wide-angle seismic data for crustal structure: Southeastern Grenville Province, *J. Geophys. Res.*, *99*, 11,687–11,704, doi:10.1029/93JB02764.